PHYSICAL REVIEW B **79**, 104421 (2009)

Spin dynamics of the frustrated easy-axis triangular antiferromagnet 2*H*-AgNiO$_2$ explored by inelastic neutron scattering

E. M. Wheeler,[1,2,*] R. Coldea,[3,1] E. Wawrzyńska,[3] T. Sörgel,[4] M. Jansen,[4] M. M. Koza,[2] J. Taylor,[5]
P. Adroguer,[3,6] and N. Shannon[3]
[1]*Clarendon Laboratory, University of Oxford, Parks Road, Oxford OX1 3PU, United Kingdom*
[2]*Institut Laue-Langevin, BP 156, 38042 Grenoble Cedex 9, France*
[3]*H.H. Wills Physics Laboratory, University of Bristol, Tyndall Avenue, Bristol BS8 1TL, United Kingdom*
[4]*Max-Planck Institut für Festkörperforschung, Heisenbergstrasse 1, D-70569 Stuttgart, Germany*
[5]*ISIS Facility, Rutherford Appleton Laboratory, Chilton, Didcot OX11 0QX, United Kingdom*
[6]*Laboratoire de Physique, École Normale Supérieure de Lyon, 46 Allée d'Italie, 69364 Lyon Cedex 07, France*
(Received 5 September 2008; revised manuscript received 29 January 2009; published 20 March 2009)

We report inelastic neutron-scattering measurements of the spin dynamics in the layered hexagonal magnet 2*H*-AgNiO$_2$, which has stacked triangular layers of antiferromagnetically coupled Ni^{2+} spins ($S=1$) ordered in a collinear alternating stripe pattern. We observe a broad band of magnetic excitations above a small gap of 1.8 meV and extending up to 7.5 meV, indicating strongly dispersive excitations. The measured dispersions of the boundaries of the powder-averaged spectrum can be quantitatively explained by a linear spin-wave dispersion for triangular layers with antiferromagnetic nearest- and weak next-nearest-neighbor couplings, a strong easy-axis anisotropy, and additional weak interlayer couplings. The resulting dispersion relation has global minima not at magnetic Bragg wave vectors but at symmetry-related soft points and we attribute this anomalous feature to the strong competition between the easy-axis anisotropy and the frustrated antiferromagnetic couplings. We have also calculated the quantum corrections to the dispersion relation to order $1/S$ in spin-wave theory by extending the work of Chubukov and Jolicoeur [Phys. Rev. B **46**, 11137 (1992)] and find that the presence of easy-axis anisotropy significantly reduces the quantum renormalizations predicted for the isotropic model.

DOI: 10.1103/PhysRevB.79.104421 PACS number(s): 75.25.+z, 75.10.Jm

I. INTRODUCTION

Quantum antiferromagnets on triangular lattices provide model systems for investigating the effects of quantum fluctuations and geometric frustration. Zero-point fluctuations are expected to be strongly enhanced for low spin and frustrated lattice geometry and may stabilize nonclassical ordered or spin liquid phases, or unconventional spin dynamics. The triangular Heisenberg antiferromagnet with first- and second-neighbor couplings J_1 and J_2 (see Fig. 1) shows strong frustration effects and a macroscopically degenerate classical ground state for $1/8 \leq J_2/J_1 \leq 1$. This was initially proposed theoretically as a candidate for a chiral spin liquid state.[1] However, perturbative expansions using a spin-wave basis[2–4] predicted that in this range of couplings quantum fluctuations do not stabilize a spin liquid state but instead lift the classical degeneracy to select a collinear stripe order pattern (see Fig. 1). Moreover, large quantum renormalizations of the spin-wave dispersion relations compared to classical have been predicted, but not probed experimentally in the absence of a good experimental model system. The recent observation of a collinear stripe-ordered ground state in the layered hexagonal antiferromagnet 2*H*-AgNiO$_2$ (Ref. 5) suggests a potential realization of the experimentally-unexplored frustrated J_1-J_2 model in the collinear phase and here we present first inelastic neutron-scattering measurements which give information about the spin gap and dispersion relations. We find that the data can be parametrized by a spin-wave dispersion relation for a J_1-J_2 triangular antiferromagnet with strong easy-axis anisotropy and weak interlayer couplings.

Delafossite materials of the type XNiO$_2$ have been generally thought of as possible two-dimensional frustrated magnets. A network of edge-sharing NiO$_6$ octahedra leads to a triangular lattice arrangement of Ni ions in planes spaced by layers of X^+ ions. There have been a variety of studies investigating the properties of compounds where $X=$Li,Na.

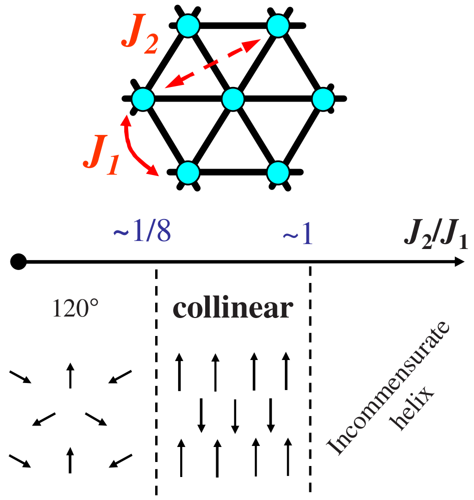

FIG. 1. (Color online) Phases of the Heisenberg triangular lattice antiferromagnet (120° coplanar order, collinear stripes and incommensurate spiral) as a function of the ratio between the first- and second-neighbor couplings, J_1 and J_2, respectively. In the collinear phase the common spin direction is spontaneously chosen and can point anywhere, it is shown here in-plane for ease of visualization.

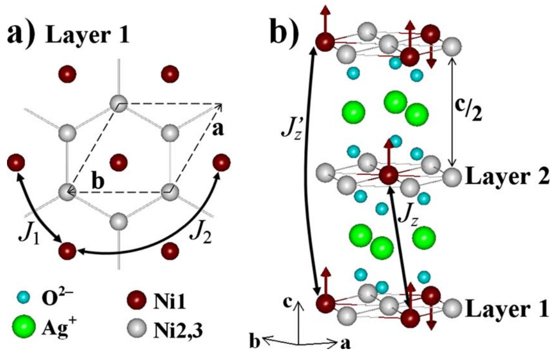

FIG. 2. (Color online) (a) Triangular lattice formed by Ni1 sites (dark brown spheres) in a hexagonal NiO_2 layer in 2*H*-$AgNiO_2$; thick arrows indicate the paths for the in-plane NN and NNN exchanges J_1 and J_2. Dashed diamond shows the crystallographic unit cell. Gray spheres are Ni2 and Ni3 sites, assumed nonmagnetic. (b) 3D view of the crystal and magnetic structure. There are two symmetry-equivalent NiO_2 layers per unit cell. Layer stacking is such that Ni1 ions sit above the center of a Ni1 triangle in the layer below. We consider two natural candidates for interlayer couplings: J_z between Ni1 ions in adjacent layers (three neighbors above and three below) and J_z' between Ni1 ions at two layers apart.

$LiNiO_2$ has shown no long-range magnetic order but experiments are hindered by the difficulty in preparing stoichiometric samples.[6] From elastic and inelastic neutron-scattering measurements, $NaNiO_2$ was found to be a spin-1/2 system with in-plane (unfrustrated) ferromagnetic interactions and weak antiferromagnetic interlayer couplings.[7]

We have recently started exploring the delafossite $AgNiO_2$, which shows frustrated antiferromagnetic in-plane interactions.[8,9] Detailed structural studies have been performed on the hexagonal polytype of $AgNiO_2$, so-called 2*H*-$AgNiO_2$ with two NiO_2 layers per unit cell [see Fig. 2(b)], as opposed to the earlier-synthesized rhombohedral 3*R* polytype[8] with a three-layer stacking sequence along *c* axis. High-resolution neutron-diffraction measurements of 2*H*-$AgNiO_2$ have observed a structural transition upon cooling below 365 K, which leads to a periodic arrangement of expanded and contracted NiO_6 octahedra.[10] This was proposed[5] to be a consequence of spontaneous charge order on the Ni sites driven by the need to lift a twofold orbital degeneracy. This leads to a strongly magnetic Ni1 site (spin-1 Ni^{2+}, 1/3 of sites) arranged in an ideal triangular lattice [see Fig. 2(a)], with the remaining 2/3 of Ni sites being $Ni^{3.5+}$ with an itinerant character.

Magnetic order occurs below $T_N = 19.7(3)$ K (Ref. 10) when the magnetic moments of Ni1 sites order in a collinear pattern of alternating ferromagnetic rows (stripes) in the triangular layers with spins pointing along the *c* axis, as shown in Fig. 3(a). A large ordered moment is found on the Ni1 sites, $1.552(7)\mu_B$ at 4 K, and no significant ordered moment could be detected on the remaining Ni2 and Ni3 sites, proposed by band-structure calculations[5] to be strongly itinerant and possibly ordered but with only a very small ($\lesssim 0.1\mu_B$) moment. So to a first approximation the coherent spin dynamics in the magnetically ordered phase is expected to be dominated by the $S=1$ Ni1 spins arranged on an ideal triangular lattice with antiferromagnetic couplings.

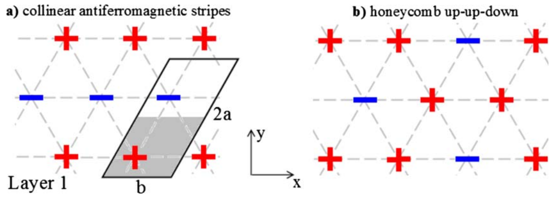

FIG. 3. (Color online) (a) Magnetic structure in a triangular layer showing the alternating stripe order of the Ni1 spins (± symbols indicate the projection of the ordered spin moments along the *c* axis). *x* and *y* labels indicate a natural orthogonal coordinate system with *x* along and *y* transverse to stripes. Solid diamond indicates the magnetic unit cell doubled along the crystallographic *a* axis compared to the chemical unit cell (light gray shaded area). The depicted magnetic structure has stripes running along the *b* axis and ordering wave vector $\boldsymbol{k} = (1/2, 0, 0)$; equivalent domains are obtained by rotating this pattern by ±60° around the *c* axis. Further neighbor couplings are required to stabilize this structure with respect to the ferrimagnetic honeycomb up-up-down pattern shown in (b).

The experimentally observed collinear stripe order in Fig. 3(a) is rather unusual for a triangular antiferromagnet (TAFM), but has been proposed to occur for the classical Ising model for finite second-neighbor couplings $J_2 \geq 0$ (Ref. 11). For the Heisenberg TAFM the collinear stripe order has also been proposed to occur as a ground state for moderate J_2 in the range $1/8 \lesssim J_2/J_1 \lesssim 1$, Ref. 3. In this range the classical ground state is macroscopically degenerate and there are many other noncollinear states degenerate with the two-sublattice collinear stripe order shown in Fig. 3(a), but zero-point quantum fluctuations are predicted to select the latter through the "order by disorder" mechanism. The large classical degeneracy is manifested also in the linear spin-wave dispersion which has many soft points with zero energy, and proper inclusion of quantum corrections leads to renormalizations of the semiclassical dispersion relation and a gapping of the nonphysical zero modes.[3] Those effects have remained experimentally largely unexplored. The recent observation[5] of a collinear stripe ordered phase in the hexagonal magnet $AgNiO_2$ suggested a possible experimental realization of the $S=1$ TAFM in the range of moderate frustration and motivated us to measure its spin dynamics in some detail. We note that the physics we are exploring here appears to be different to that in the recently explored $S=5/2$ TAFM $CuFeO_2$ which has a related but different collinear structure of alternating "double stripes" (↑↑↓↓) stabilized by strong three-dimensional (3D) and third-neighbor in-plane couplings.[12] In 2*H*-$AgNiO_2$ the magnetic structure is a (simpler) single-stripe pattern ↑↓ with only two in-plane sublattices possibly stabilized by fewer exchanges (only first and second in-plane neighbors) and easy-axis anisotropy.

The plan of this paper is as follows. The following Sec. II gives details of the inelastic neutron-scattering experiments to probe the powder-averaged spin dynamics and the results are presented in Sec. III. In the following Sec. IV A the data are parametrized in terms of an empirical sinusoidal dispersion model with minima at magnetic Bragg wave vectors and different zone boundary energies along the three orthogonal directions in the Brillouin zone (BZ); this parametrization gives a gapped and predominantly two-dimensional dispersion relation. In the following Sec. IV B the data are compared with linear spin-wave theory for a microscopic spin Hamiltonian for the localized Ni spins that includes both first- and second-neighbor antiferromagnetic couplings in the triangular layers, easy-axis anisotropy modeled by a single-ion term, and different models for interlayer couplings consistent with the crystal structure; a minimal spin Hamiltonian is proposed. In the following Sec. IV C we consider how magnon interactions included at order $1/S$ in spin-wave theory renormalize the dispersion relation and find slightly renormalized values for the proposed spin interactions. Finally, the results for the spin dynamics are summarized and discussed in the concluding Sec. V. Technical details of the spin wave calculations for coupled easy-axis triangular layers are given in Appendix A. Details of the derivation of the $1/S$ quantum corrections to the dispersion relation for an easy-axis triangular antiferromagnet are given in Appendix B.

II. EXPERIMENTAL DETAILS

Powder samples of the hexagonal polytype of $AgNiO_2$ were prepared from Ag_2O and $Ni(OH)_2$ using high oxygen pressures (130 MPa) as described in Ref. 9. The samples used for the inelastic neutron experiments were part of the same batch used in previous neutron-diffraction measurements[10] performed on about half of the total sample quantity, which revealed a high-purity hexagonal phase ($<1\%$ admixture of the rhombohedral polytype). The crystal structure of $2H$-$AgNiO_2$ is shown in Fig. 2(b) and is hexagonal with space group $P6_322$ (no. 182) and lattice parameters $a=5.0908(1)$ Å and $c=12.2498(1)$ Å (Ref. 5). Ni ions are located inside hexagonal (ab) layers and there are three distinct crystallographic sites: Ni1 which sit inside slightly expanded NiO_6 octahedra arranged in a periodic triangular lattice of spacing a, surrounded by a honeycomb of contracted NiO_6 octahedra which contain the Ni2 and Ni3 sites, see Fig. 2(a).

The powder-averaged magnetic excitation spectrum was probed using two direct-geometry time-of-flight neutron spectrometers: MARI, at the ISIS Facility in the U.K., and IN6, at the Institute Laue-Langevin in France. Measurements on MARI showed that the full dynamic range of the spin excitations extended only up to 7.5 meV so could be accessed with incident neutrons of energy $E_i=18$ meV, which gave an energy resolution of 0.61(1) meV (FWHM) on the elastic line. Higher-resolution measurements to probe the low-energy part of the spectrum were made using IN6 operated with incident neutrons of energy $E_i=3.86$ meV, which gave a measured energy resolution of 0.142(1) meV (FWHM) on the elastic line. The sample was cooled using either a closed-cycle refrigerator (MARI, base temperature 4.7 K) or orange cryostat (IN6, base temperature 1.8 K). Measurements were made at the lowest temperatures in the magnetically ordered phase, near the ordering transition and at high temperatures in the paramagnetic phase.

For the MARI experiment 23 g of powder were placed in an annular-shaped sachet to minimize absorption. For the low-energy IN6 measurements a similar powder quantity was placed in a plate-shaped container angled at 45° to the incident beam and the data were corrected for neutron absorption effects using a numerical calculation for plate-shaped samples. The scattering intensities from both instruments have been converted into absolute units of $S(Q,\omega)$ of mbarns/meV/sr/Ni1 by normalizing the raw counts to the sample mass and to the measured scattering intensities from a vanadium standard.

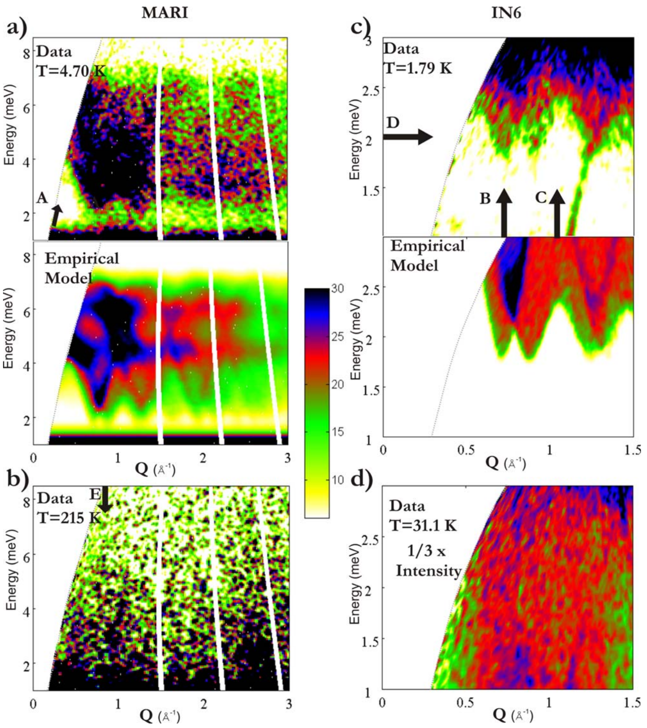

FIG. 4. (Color online) Powder-averaged magnetic excitation spectrum in $2H$-$AgNiO_2$ in the magnetically ordered phase [top panels (a) and (c)] showing a band of spin excitations above a small gap, (b) in the paramagnetic phase at high temperature showing an overdamped signal and (d) slightly above the magnetic ordering temperature showing a filling-in of the spin gap [compare with (c)]. Data are raw counts collected after 35 h (a) and 4.5 h (c) and normalized to absolute units as described in the text. The streak of intensity in panel (c) near $Q=1.1$ Å^{-1} is nonmagnetic and attributed to an acoustic phonon dispersing out of the (002) structural Bragg peak. Middle panels show the intensity distribution for the empirical dispersion model in Eqs. (1) and (3). The calculations include convolution with the instrumental resolution, the magnetic form factor, polarization factor, and an estimate of the nonmagnetic background to be directly compared with the data in the panels immediately above. Thick bold arrows labeled A–E indicate the location of scans plotted in Figs. 5(A)–5(E) and the gray dotted lines in all plots indicate the low-Q edge of the measured region.

III. MEASUREMENTS AND RESULTS

An overview of the measured inelastic neutron-scattering data is shown in Fig. 4. Below the Néel ordering temperature $T_N=19.7(3)$ K a strong band of scattering is clearly observed at low energies, E, and low wave vectors, $Q=|\mathbf{Q}|$,

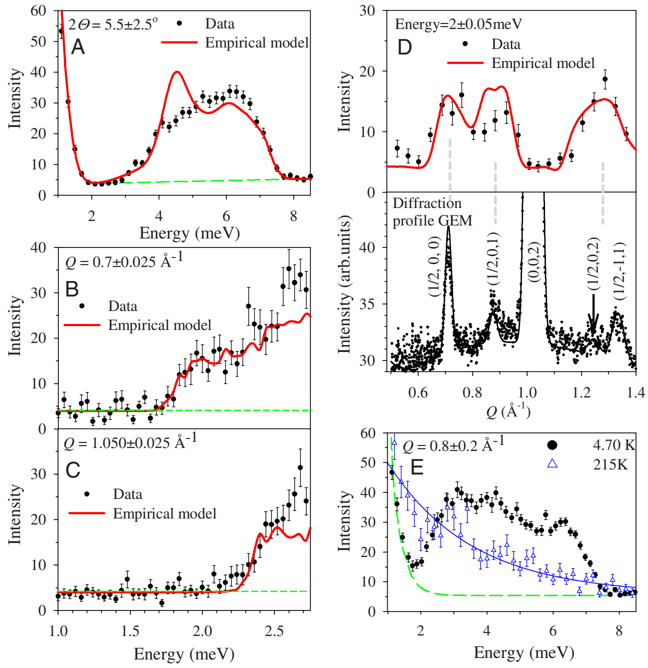

FIG. 5. (Color online) Scans through the powder data along special directions labeled A–E in Fig. 4. Scan D shows that there is structure in the low-energy inelastic signal for wave vectors where Bragg peaks occur (lower panel in D shows diffraction data indicating magnetic Bragg peaks). The energy scan E integrates over a broad Q range and shows the full bandwidth of the magnetic excitations: low temperature data (solid points) are replaced in the paramagnetic phase at high temperatures by an overdamped signal (triangles, solid line is a guide for the eyes). In panels A–D the thick solid lines show calculations for the sinusoidal dispersion model in Eqs. (1) and (3) with dispersion relations plotted in Fig. 7. The green dashed lines indicate the estimated nonmagnetic background.

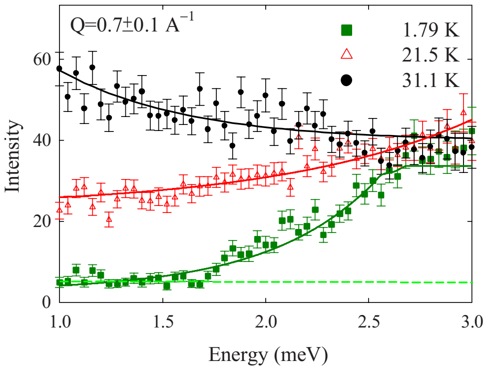

FIG. 6. (Color online) Energy scan at the minimum gap wave vector showing a filling of the gap upon heating above the magnetic ordering temperature. Solid lines are guides for the eyes and the dashed line indicates the estimated nonmagnetic background.

+[Figs. 4(a) and 4(c)], attributed to magnetic excitations. The intensity of the signal decreases with increasing wave vector Q, confirming its magnetic character. The intensity starts above a small gap of 1.8 meV and extends up to 7.5 meV, above which the signal decreases to background level. This energy scale for the magnetic excitations spectrum is consistent with susceptibility measurements which observed a Curie-Weiss temperature of $k_B\theta = -9.2$ meV (Ref. 10). Energy scans through the data at constant wave vectors showing the low energy gap and the full extent of the scattering are shown in Figs. 5(A) and 5(E) (solid points). The dashed line in those plots indicates the estimated nonmagnetic background, obtained by a smooth interpolation of the signal observed at energies below and above the magnetic signal. The energy gap to magnetic excitations fills up upon heating through the Néel temperature [compare Fig. 4(c) with Fig. 4(d) and scans shown in Fig. 6]. The structured band of magnetic scattering is replaced as expected by an overdamped signal in the paramagnetic phase at high temperatures; compare Fig. 4(a) with Fig. 4(b) and various scans in Fig. 5(E).

At the lowest temperatures the boundaries of the magnetic scattering show considerable structure which can be used to impose constraints on the underlying dispersion relation. In particular information is contained in the gap, extent of bandwidth, slope of low-Q dispersion up to the first minimum gap [see Fig. 4(a)] and the low-energy dispersion (~10% of bandwidth) between subsequent minimum gap wave vectors [see Fig. 4(c)]. The powder data are a spherical average of the dispersions along all directions in reciprocal space weighted by the neutron structure factor, so the low-energy boundary of the powder data corresponds to the dispersion along some direction in reciprocal space which has the minimum energy at a given Q. In general the spin-wave dispersion has global minima at magnetic Bragg wave vectors and here strong low-energy scattering is expected. This is consistent with the data in Fig. 4(c) showing clear lobes of magnetic scattering intensity coming down in energy near wave vectors 0.7 and 0.9 Å^{-1} where the first two magnetic Bragg peaks (1/2,0,0) and (1/2,0,1) occur; a constant energy scan near the gap minimum is shown in Fig. 5(D). Inelastic intensity occurs near the same wave vectors as magnetic Bragg peaks in the diffraction pattern shown in Fig. 5(D) bottom panel (data from the GEM diffractometer at ISIS). The low-energy boundary of the scattering is clearly modulated as a function of wave vector and the onset energy varies as a function of wave vector Q as illustrated by comparing energy scans in Figs. 5(B) and 5(C).

IV. ANALYSIS

The modulations observed in the lower boundary of the magnetic scattering indicate strongly dispersive excitations, however, in principle it is not possible to extract precise dispersion relations from the powder data, which represents an average along all directions in reciprocal space. Nevertheless, if the dispersion is highly asymmetric along different directions and if in-plane and out-of-plane lattice parameters are sufficiently different then the lower boundary of the scattering can be identified over certain Q ranges with the dispersion along specific directions in reciprocal space, so one may impose certain constraints on the dispersion model. Following this approach we have found two models for the dispersion relation that could both explain the observed wave-vector dependence of the boundaries of the powder-averaged spectrum and present them in the following.

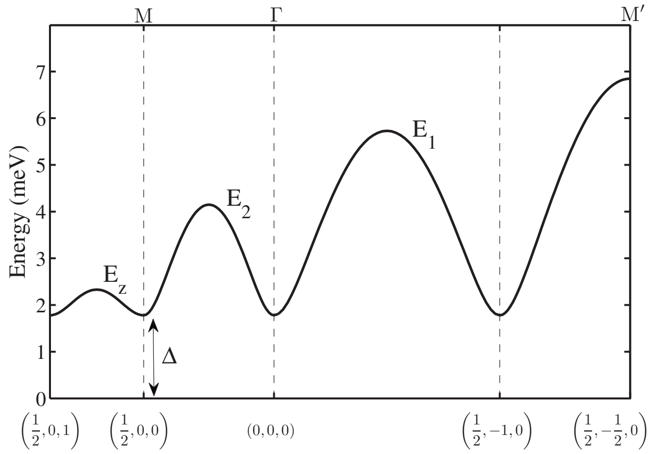

FIG. 7. Sinusoidal dispersion relation in Eq. (1) plotted along symmetry directions in the Brillouin zone in Fig. 8(b) (dashed lines). Dispersion parameters are $\Delta = 1.78$ meV, $E_1 = 5.73$ meV, $E_2 = 4.15$ meV, and $E_z = 2.33$ meV.

A. Parametrization by an empirical sinusoidal dispersion model

We first consider a parametrization of the data by an empirical sinusoidal dispersion model with a finite gap Δ above the magnetic Bragg peaks and different zone boundary energies along the three orthogonal directions in the Brillouin zone: E_1 along the magnetic stripe direction, E_2 transverse to stripes in the plane, and E_z in the interlayer direction. In detail we consider the following *empirical form* for the dispersion relation $\omega_{\boldsymbol{Q}}$:

$$(\omega_{\boldsymbol{Q}})^2 = \Delta^2 + (E_1^2 - \Delta^2)\sin^2(Q_x a/2) + (E_2^2 - \Delta^2)\sin^2(Q_y a\sqrt{3}/2) + (E_z^2 - \Delta^2)\sin^2(Q_z c/2), \tag{1}$$

where Q_x, Q_y, and Q_z are components (in Å^{-1}) of the wave vector transfer $\boldsymbol{Q}$ in an orthogonal coordinate system with x along the magnetic stripes, y transverse to stripes in plane, and z normal to the planes. The transformation to wave vector components (h,k,l) in units of the reciprocal lattice of the hexagonal unit cell is given by

$$Q_x = -\frac{2\pi}{a}k,$$

$$Q_y = \frac{2\pi}{a\sqrt{3}}(2h+k),$$

$$Q_z = \frac{2\pi}{c}l. \tag{2}$$

Figure 7 shows a plot of this dispersion relation along various symmetry directions in the Brillouin zone and Fig. 8(b) shows a 2D contour map of the dispersion. The minimum gap Δ is reached at the origin and at all magnetic Bragg peak positions $(H,K,L) \pm \boldsymbol{k}$ with $\boldsymbol{k} = (1/2,0,0)$ the ordering wave vector and H, K and L integers. In order to compare this dispersion relation with the data one needs also a model for the neutron-scattering cross section. We assume the following simple form for the one-magnon cross section:

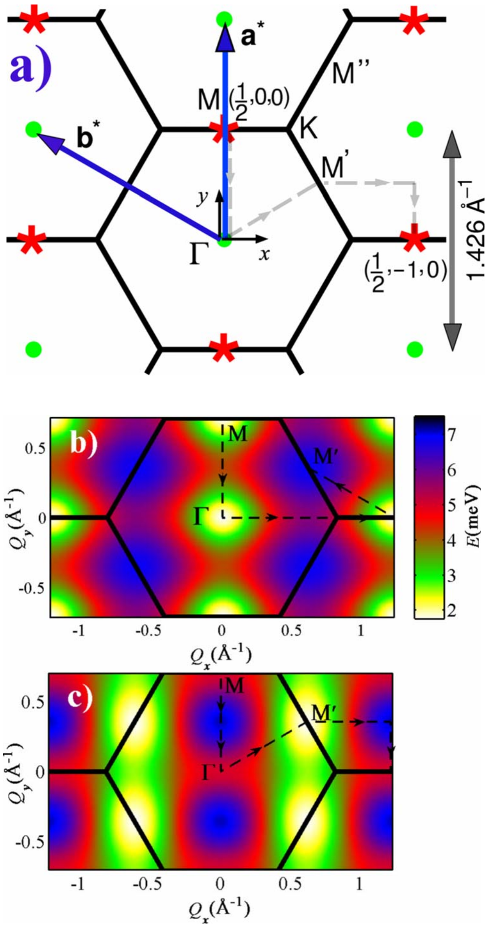

FIG. 8. (Color online) (a) Reciprocal basal plane of 2*H*-AgNiO$_2$ showing the Brillouin zone edges (thick line hexagons), zone centers (solid points), and locations (stars) of magnetic Bragg peaks from the ordered domain shown in Fig. 3(a) with stripes along the $\boldsymbol{b}$ axis. Labels Γ, M, and K indicate special symmetry points in the hexagonal Brillouin zone (M' and M'' are Bragg peak positions for equivalent ordered domains with stripes along $\boldsymbol{a}+\boldsymbol{b}$ and $\boldsymbol{a}$, respectively). Dashed gray lines show directions along which the dispersion is plotted in Fig. 10. Arrows labeled x and y indicate the natural orthogonal coordinate system used for the empirical dispersion model in Eq. (1). [(b) and (c)] Color contour maps of the dispersion in the (ab) plane in the two models consistent with the data: (b) the empirical parametrization with a sinusoidal dispersion plotted in Fig. 7 and (c) the linear spin-wave model for J_1–J_2 triangular layers with easy axis and interlayer couplings in Fig. 10(d) (dashed line). Note that in model (b) the minimum gap occurs at the magnetic Bragg wave vector M, whereas in model (c) the minimum gap occurs at the soft point M'.

$$S^{xx}(\boldsymbol{Q},\omega) = S^{yy}(\boldsymbol{Q},\omega) = \mathcal{C}\frac{S}{2}(\omega_{\boldsymbol{k}})_{\max}\frac{1-\gamma_{\boldsymbol{Q}}}{\omega}G(\omega-\omega_{\boldsymbol{Q}}). \tag{3}$$

Here $\mathcal{C}$ is an overall scale factor and $(1-\gamma_{\boldsymbol{Q}})$ is a geometric factor to concentrate the intensity near the antiferromagnetic Bragg peak wave vectors $(H \pm 1/2, K, L)$ with H, K, L integers, $\gamma_{\boldsymbol{Q}} = \cos(Q_x a/2)\cos(Q_y a\sqrt{3}/2)$. The $1/\omega$ factor is a characteristic energy dependence of the spin-wave structure

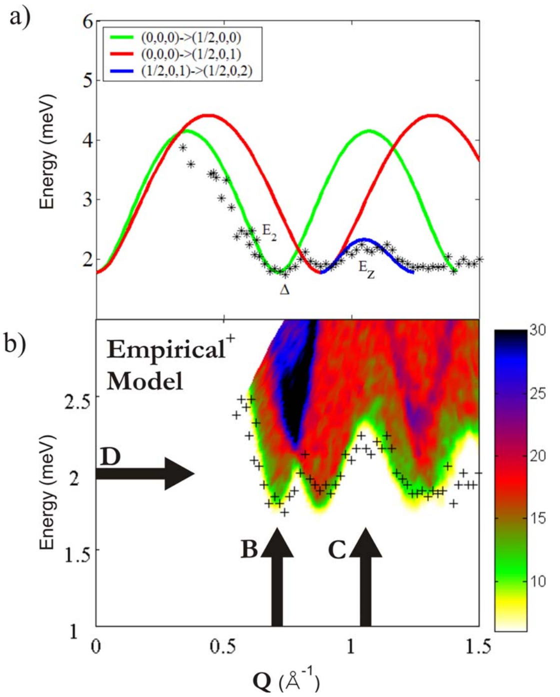

FIG. 9. (Color online) (a) Dispersion relations for the empirical sinusoidal model in Eq. (1) along various directions involved in defining the low-energy edge of the powder-averaged spectrum. (b) Corresponding powder-averaged spectrum. Stars in both panels are the experimentally determined low-energy edge of the magnetic scattering. Thick arrows indicate location of scans B, C, and D in Fig. 5.

factor for antiferromagnets and $(\omega_{\boldsymbol{k}})_{\max}$ is the maximum magnon energy for all wave vectors $\boldsymbol{k}$, and is introduced here for dimensionality purposes. $S=1$ is the spin quantum number. Equation (3) includes the fact that spin fluctuations occur in the plane transverse to the ordered spin direction in a collinear antiferromagnet, so x and y refer to two orthogonal directions in the hexagonal ab plane and z is along c. This form is a generic structure factor for many simple spin-wave models of collinear antiferromagnets. Here $G(\omega-\omega_{\boldsymbol{Q}})$ is a Gaussian function which models the instrumental resolution.

A spherical average of the intensity distribution of Eq. (3) including the neutron polarization factor, magnetic form factor for Ni^{2+} ions [as in Eq. (A5)], and an estimated additive nonmagnetic background (including the incoherent elastic line) was compared to the data and the overall comparison is shown in the middle panels of Fig. 4. The overall bandwidth and the observed structure in the data at low energies is well reproduced by this model for gap $\Delta=1.78(5)$ meV, $E_1=5.73(4)$ meV, $E_2=4.15(6)$ meV and $E_z=2.33(5)$ meV in Eq. (1). The maximum magnon energy is $(\omega_{\boldsymbol{k}})_{\max}=7.0$ meV and an overall scale factor $\mathcal{C}\simeq 0.35$ in Eq. (3) gives intensities comparable to data.

To analyze the agreement quantitatively we first show in Fig. 9(a) how the lower boundary of the powder-averaged magnetic signal can be identified over certain wave-vector ranges with the dispersion along particular directions in reciprocal space. In particular the observed sharp low-Q dispersion up to the first gap minimum near $Q_M=0.7$ Å^{-1} in Fig. 4(a) is attributed to the dispersion between the origin $\Gamma(000)$ and the closest magnetic Bragg peak at $M(1/2,0,0)$; scan A along the direction indicated by the bold arrow in Fig. 4(a) is therefore very sensitive (at low energies) to the ΓM dispersion and a fit to this scan shown in Fig. 5(A) gives $E_2=4.15\pm 0.06$ meV, the zone boundary along the direction transverse to stripes in plane. To explain the observed full extent of the bandwidth up to 7.5 meV another dispersion larger in magnitude is required and this is assigned to the direction along the stripes, E_1, since the interlayer dispersion bandwidth $E_z-\Delta$ is assumed to be small. Quantitative fits give $E_1=5.73\pm 0.04$ meV. The energy scan in Fig. 5(B) is sensitive to the gap above the magnetic Bragg wave vector, obtained as $\Delta=1.78(5)$ meV. The energy scan in Fig. 5(C) is at a wave vector corresponding to the midpoint between two subsequent Bragg wave vectors along the c axis, (1/2,0,1) and (1/2,0,2) [see Fig. 9(a)], so this scan is sensitive to the interlayer zone boundary and fits give $E_z=2.33\pm 0.05$ meV, thus obtaining the last parameter of the empirical dispersion relation.

Figure 9 shows in more detail the agreement between the experimentally determined onset of the magnetic scattering (stars) and the empirical model (various solid lines) in panel (a) and the calculated powder-averaged spectrum in panel (b). The onset points were determined from scans through the measured powder data at fixed wave vector Q and locating the energy where the magnetic intensity was above a minimum threshold value. The model reproduces well the shape of the lower edge of the scattering. Fits to specific scans shown in Figs. 5(A)–5(D) give good account of the onset and upper boundary of the scattering. The form of the intensity distribution within the excitation band is not replicated in detail, as seen for example in Fig. 5(A) where the simulation gives a more pronounced trough in the intensity in the middle of the band. This is almost certainly due to the oversimplification of the model.

B. Parametrization in terms of an easy-axis Heisenberg model on a triangular lattice

The empirical sinusoidal dispersion model considered in Sec. IV A is the simplest dispersion model that can be used to parametrize and explain quantitatively the observed dispersion of the boundaries of the powder-averaged magnetic inelastic scattering. This analysis suggested that the dispersion relation is gapped and predominantly two dimensional. Here we compare the data quantitatively with predictions of linear spin-wave theory for a microscopic model of coupled triangular layers where we include antiferromagnetic in-plane couplings for the first- and second-neighbor exchanges J_1 and J_2, an easy-axis anisotropy and allow for both first- and second-layer couplings J_z and J_z', as shown in Figs. 2(a) and 2(b). Specifically, we consider the spin Hamiltonian

$$\mathcal{H}_0=\sum_{\mathrm{NN}} J_1\boldsymbol{S}_i\cdot\boldsymbol{S}_j+\sum_{\mathrm{NNN}} J_2\boldsymbol{S}_i\cdot\boldsymbol{S}_l-\mathcal{D}\sum_i (S_i^z)^2 + \sum_{\mathrm{InterlayerNN}} J_z\boldsymbol{S}_i\cdot\boldsymbol{S}_k+\sum_{\mathrm{InterlayerNNN}} J_z'\boldsymbol{S}_i\cdot\boldsymbol{S}_n, \qquad (4)$$

where the spin is $S=1$, NN and NNN stand for nearest-

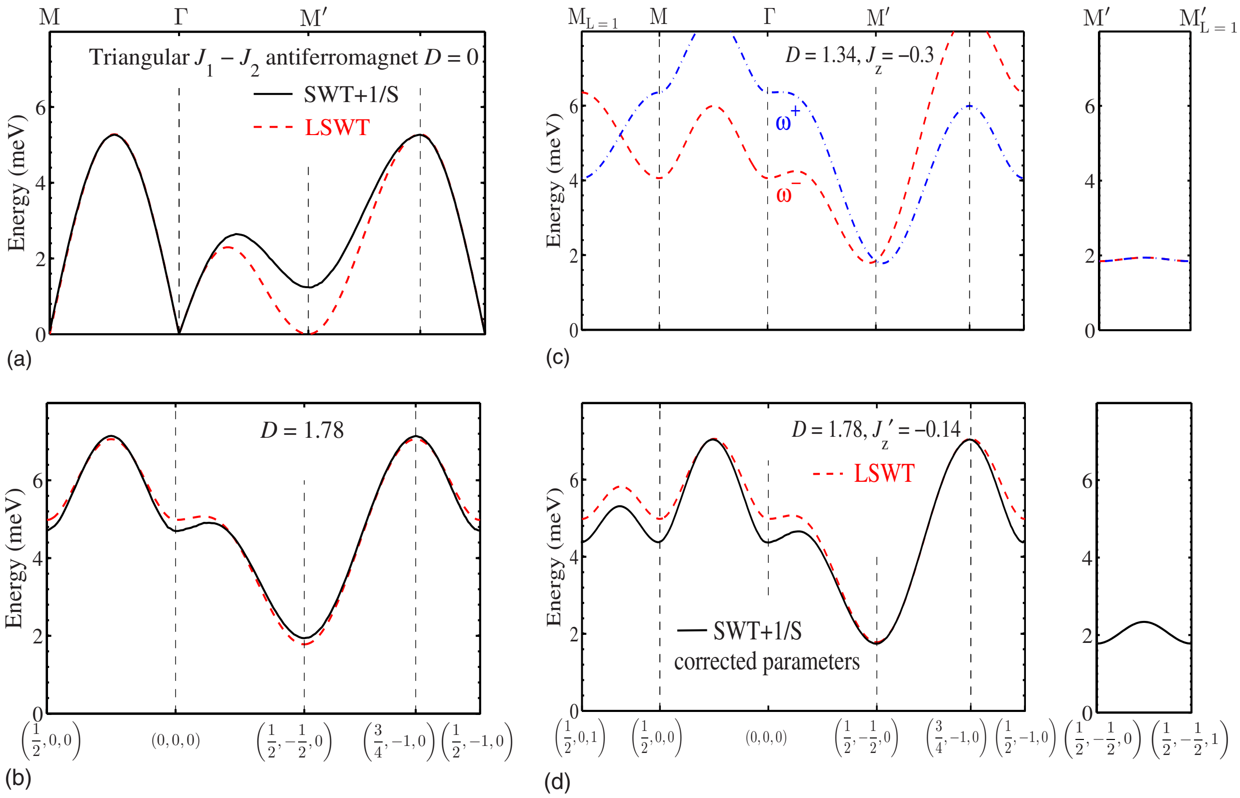

FIG. 10. (Color online) Dispersion relation for the stacked triangular antiferromagnetic layers within LSWT (dashed lines) and SWT $+1/S$ (solid lines) for various values of the parameters. The dispersion is plotted along high-symmetry directions in reciprocal space [dashed line path in Fig. 8(a)], top labels are high symmetry points in the Brillouin zone. (a) Triangular lattice with antiferromagnetic couplings $J_1 = 1.32$ meV, $J_2 = 0.15 J_1$ and no anisotropy. $1/S$ quantum corrections have a large effect at the soft point M'. (b) Same as (a) but with easy-axis anisotropy $\mathcal{D} = 1.78$ meV; $1/S$ corrections are much smaller. (c) Triangular layers with easy-axis anisotropy and coupled by NN interlayer exchange $J_z = -0.3$ meV. This leads to two incommensurate spin-wave modes with very little interlayer dispersion near the gap minimum (last panel in the row), not consistent with data. (d) Triangular layers with anisotropy coupled by second-layer exchange $J'_z = -0.14$ meV; this model gives the best fit to the data. Dashed (solid) line shows best fit using LSWT (SWT$+1/S$) with parameter values given in Table I.

neighbor and next-nearest-neighbor and each spin pair is counted once in the summation. The third term is an easy-axis anisotropy, needed to select the ordering spin direction along c, and to generate a spin gap in the spectrum. In the absence of a clear physical picture of the origin of the anisotropy, we have chosen a single-ion form for this term. We anticipate that an exchange anisotropy $(\delta J)^z S_i^z S_j^z$ would have qualitatively similar effects. Both in-plane exchanges are antiferromagnetic $J_1, J_2 > 0$ whereas the interlayer couplings are taken to be ferromagnetic $J_z, J'_z < 0$, to stabilize the observed magnetic structure shown in Fig. 2(b).

We have calculated the spin-wave dispersion and dynamical correlations for the spin Hamiltonian (4) in the large S limit using the standard Holstein-Primakoff formalism and details are given in Appendix A with the dispersion relations in Eq. (A2). To illustrate the effect of the various terms in the Hamiltonian we plot the dispersion for a triangular lattice with no anisotropy in Fig. 10(a) (dashed line). The linear spin-wave dispersion has zero modes not only at the magnetic Bragg peak position M for the specific ordered magnetic domain, but also at soft points such as M' in Fig. 8 which are Bragg peak positions for the symmetry-equivalent domains (there are three possible magnetic domains related by a threefold rotation around the c axis).

The presence of such unphysical gapless modes is a consequence of the macroscopic ground-state degeneracy at the classical level and including $1/S$ corrections [Fig. 10(a), solid line] generates a gap at the soft points but preserves a gapless Goldstone mode at the Bragg wave vectors.[3] The situation is completely different in the presence of an easy-axis anisotropy which generates a gap everywhere [see Fig. 10(b)]; the gap at the Bragg wave vector increases very rapidly as a power law, whereas at the soft point increases only linearly with anisotropy, so above some threshold anisotropy value the minimum gap is no longer at the magnetic Bragg wave vector M, but moves to the soft point M'.

Coupling the layers by a NN exchange $J_z < 0$ (ferromagnetic) has the effect of splitting the dispersion into two modes [see Fig. 10(c)], corresponding to acoustic and optic magnon modes between the two layers in the unit cell. The gap minimum is no longer at the commensurate soft point M' but at incommensurate positions symmetrically displaced from M' along the magnetic stripe direction; see Fig. 10(c). The incommensurate position of the gap minimum varies linearly with $|J_z|$ for small J_z and it originates physically from the fact that hopping of magnons is somewhat frustrated as an up spin in the bottom layer interacts through J_z with two up and one down spin in the layers above and

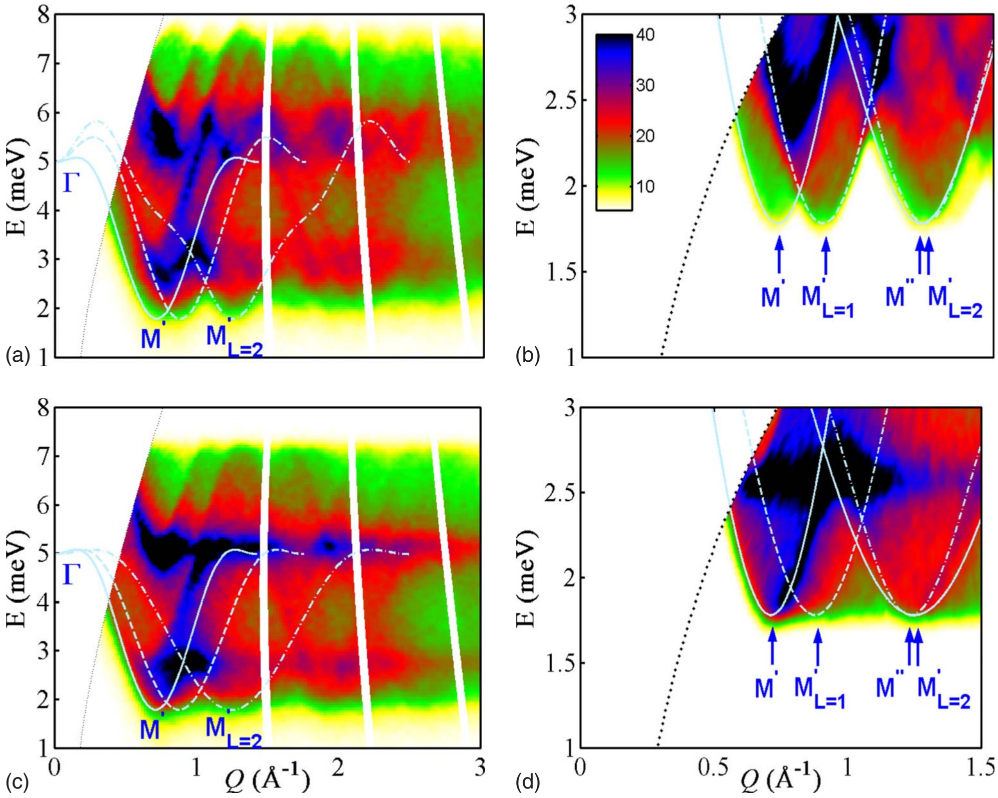

FIG. 11. (Color online) Powder averaged spin-wave spectrum for easy-axis triangular layers with/without (top/bottom) interlayer couplings. Left panels to be compared with Fig. 4(a) and right panels to Fig. 4(c). The parameters are $J_1=1.32$ meV, $J_2=0.15J_1$, $\mathcal{D}=1.78$ meV, $J_z=0$, and $J_z'=-0.14$ meV (top panels) or $J_z'=0$ meV (bottom panels). The calculations contain an additive flat background. The various lines overplotted onto the intensity color maps show the dispersion along the directions from the origin Γ point to the closest soft points at $M'(1/2,-1/2,0)$ (and the $L=1$ and $L=2$ versions of this) and $M''(1,-1/2,0)$, with minima at wave vectors indicated by the vertical arrows in the right panels. The dispersion at the lower boundary of the scattering in (b) is very similar to the data in Fig. 4(c) and are attributed to the weak interlayer couplings [no interlayer dispersion is present in (d) calculated for decoupled layers]. The dotted lines at low-Q mark the left edge of the region probed by the experiments.

below; see Fig. 15(b). Moreover, there is very little interlayer dispersion of the gap minimum, i.e., between soft points M' with different L values [see Fig. 10(c) last panel], also due to frustration in the magnon interlayer hopping at those wave vectors.

Both of these features, incommensurate minima in the dispersion displaced (in-plane) away from M' and very weak interlayer dispersion of the gap minimum, are inconsistent with the data, which shows minima in the scattering at wave vectors very close to those corresponding to the commensurate M' point and a significant (∼10% of the total bandwidth) interlayer dispersion of the gap minimum. This suggests that the observed interlayer dispersion is not due to the nearest-neighbor interlayer exchange J_z but is due to another interlayer coupling.

To find a possible explanation for the observed interlayer dispersion we now assume $J_z=0$ and consider the effects of a ferromagnetic second-layer coupling J_z' straight up along the c axis; see Fig. 2(b). The resulting dispersion is plotted in Fig. 10(d) (dashed line); there is a single mode with essentially the same features as for decoupled triangular layers [see Fig. 10(b)] with global minima at the commensurate soft point M' but now there is a modulation in the energy as a function of L value to first order in J_z'. This model can account for all observed dispersions in the boundaries of the powder-averaged spectrum and the calculation for the best fit parameter set is plotted in Figs. 11(a) and 11(b) to be compared with data in Figs. 4(a)–4(c).

In the calculation we used the dynamical correlations in Eq. (A3), included polarization factor and magnetic form factor as in Eq. (A5), and performed a spherical average. An overall intensity scale factor $\mathcal{C}\sim 0.57$ gives intensities comparable to data; we do not attach special significance to this value except that it is comparable to the LSWT prediction of $\mathcal{C}=1$. The intensity distribution is also reasonably well captured by the model as shown by the typical scans in Fig. 12; any differences compared to the data may be due to interactions beyond the minimal spin Hamiltonian considered.

To obtain quantitative values for the model parameters we have used the fact that various parts of the spectrum are mostly sensitive to only one parameter; in particular the gap depends only on anisotropy via $\Delta_{M'}=2S\mathcal{D}(1-\frac{1}{2S})$, the upper boundary of the spectrum is mostly sensitive to the main coupling J_1, the magnitude of the low-energy dispersion between the gap minima with $L=1$ and 2 is given by $4S|J_z'|$. The remaining parameter J_2 is extracted from the slope of the low-Q dispersion up to the first gap minimum. Specifically, a fit to scan B at the minimum gap [Fig. 12(B)] gives the

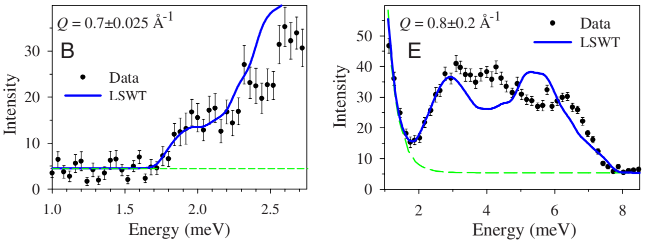

FIG. 12. (Color online) Comparison between data (filled points) and the linear spin-wave model for easy-axis triangular layers (solid lines). Dashed lines show the estimated nonmagnetic background and parameters are as in Fig. 11(a).

anisotropy $\mathcal{D}$, scan C probes the interlayer dispersion so gives J_z', fits to scans A and E upper boundary [Fig. 12(E)] give the main coupling J_1 and fits to scan A lower boundary give the secondary coupling J_2.

The best fit values for the parameters obtained this way are shown in Table I. The calculated powder-averaged spectrum is shown in Figs. 11(a) and 11(b) and compares well with the data in Figs. 4(a)–4(c). To emphasize the sensitivity of the data to the 3D couplings we also plot in Figs. 11(c) and 11(d) the powder-averaged spectrum assuming decoupled layers, which reproduces the bandwidth, gap, and slope of the low-Q dispersion up to the first gap minimum but not the low-energy dispersion (~10% of bandwidth) between subsequent minimum gap wave vectors.

In the above analysis we neglected the NN interlayer coupling J_z since the powder data are not very sensitive to its presence; in particular a finite J_z produces only a negligible interlayer dispersion of the gap minimum (dispersion appears only at order $J_z^2/\mathcal{D}$ for small J_z). Using the fact that a finite J_z produces a small incommensurate shift of the minimum gap wave vector an upper bound for the maximum J_z that would still be consistent with the data can be estimated as $|J_z| \lesssim 0.25$ meV.

Within the minimal model we considered in Eq. (4) the estimated values of the interaction parameters would give a Curie-Weiss constant expected in a high-temperature susceptibility measurement on a powder sample as[13]

$$k_B\theta = -\frac{1}{3}S(S+1)(6J_1 + 6J_2 + 2J_z') = -5.9\ \text{meV}.$$

This is smaller than, but comparable to, the experimental value of $k_B\theta = -9.2$ meV extracted from high-temperature susceptibility data[10] and the difference may be due to other interactions beyond the minimal model we have considered to explain the dispersive boundaries of the powder data.

C. Spin-wave theory with 1/*S* corrections for easy-axis triangular layers

In the absence of anisotropy the 2D triangular J_1-J_2 antiferromagnet in the collinear phase has been shown to exhibit a strong renormalization of the dispersion relation due to quantum fluctuations. Including the effects of fluctuations to order $1/S$ in spin-wave theory[3] generates a gap at the soft points where the LSWT calculation predicts unphysical gapless modes, as illustrated in Fig. 10(a) solid line is SWT $+1/S$ and dashed is LSWT.

In Appendix B we have calculated the $1/S$ corrections to the dispersion relation for the triangular antiferromagnet when an easy-axis anisotropy is also present and the results are plotted in Fig. 10(b). The energy at the soft point is now only marginally renormalized up in energy because the easy-axis anisotropy generates a gap in the spectrum and this reduces significantly the zero-point quantum fluctuation effects. Using the 2D dispersion relation at order $1/S$ and including also the interlayer coupling the best parameter values obtained from comparison to the data are very similar to those found using LSWT and are shown in Table I. The dispersion relation at order $1/S$ for these parameters is plotted in Fig. 10(d) (solid line) and is very similar to the LSWT dispersion for the uncorrected parameters (dashed line). The powder-averaged spectrum is also similar to Figs. 11(a) and 11(b) for the uncorrected parameters and is therefore not reproduced here.

In converging to the above set of parameter values for the microscopic Hamiltonian we have used two constraints imposed by the data (i) the interlayer dispersion is relatively small, ~10% of the bandwidth, as inferred from the observed small dispersion in the low-energy boundary of the magnetic inelastic scattering, and (ii) the spin gap is relatively large, ~30% of the bandwidth, which in turn implies a relatively large easy-axis anisotropy. Specifically, subtracting the estimated interlayer dispersion magnitude from the observed maximum energy leads us to search for a 2D dispersion shape where the gap energy divided by the maximum, i.e., the reduced gap $\Delta/\omega_{\max}$, is ~25%.

The dispersion of the microscopic Hamiltonian in Eq. (4) has the minimum either at the Bragg peak position M, or at the soft point M'. This places a strong constraint on model parameters, since both reduced gaps must be at or above the threshold value of 25%, with at least one gap precisely at the

TABLE I. Table of best fit values for easy-axis Heisenberg model applied to AgNiO$_2$. In both cases fits are obtained by comparing the spin-wave dispersion calculated within linear spin-wave theory, and including leading interaction corrections, with the envelope of the powder-averaged spin structure factor $S(Q,E)$ measured by inelastic neutron scattering. We set $S=1$ and $J_z \equiv 0$ in all fits. All exchange parameters are given in meV.

	S	J_1	J_2	$\mathcal{D}$	J_z	J_z'
LSWT	1	1.32(5)	0.15(3)	1.78(5)	0	−0.14(2)
SWT+1/*S*	1	1.35	0.15	1.59	0	−0.14

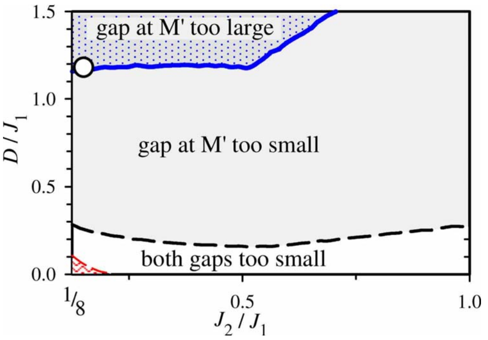

FIG. 13. (Color online) Constraints on the parameters J_2/J_1 and $\mathcal{D}/J_1$ determined from the spin gap measured in inelastic neutron-scattering experiments. Gaps at M and M' are calculated within SWT+$1/S$ discussed in Appendix B, and normalized to the maximum energy for spin excitations. The upper solid line divides solutions where the calculated gap at M' is larger than that seen in experiment, from those where it is smaller. The point $J_2/J_1 \approx 0.15$, $\mathcal{D}/J_1 \approx 1.2$ which gives the best fit overall fit to experiment is marked with an open circle. The region of small $\mathcal{D}$ for which neither the gap at M nor M' are large enough to fit experiment is bounded by a dashed line. Linear spin-wave calculations give similar lines, slightly shifted. (The small region of parameter space $\mathcal{D}/J_1 \gtrsim 0$, $J_2/J_1 \gtrsim 1/8$ for which spin-wave theory is ill-conditioned is shown by the red hatched area.)

threshold. In Fig. 13 we map out these constraints for $(J_2/J_1, \mathcal{D}/J_1)$ parameter space, with gaps calculated using spin-wave theory with $1/S$ corrections, as described in Appendix B. Possible solutions lie on the solid line dividing solutions where the reduced gap $\Delta_{M'}/\omega_{\max} > 25\%$ from those where $\Delta_{M'}/\omega_{\max} < 25\%$.

On this line other features in the data such as the observed slope of the low-Q dispersion further narrow down possible parameter values, leading to the best fit values. So within the minimal microscopic Hamiltonian considered the requirement for quantitative agreement for the absolute gap relative to the maximum energy requires a relatively large anisotropy, and in this case the dispersion minimum is at the soft point M' as illustrated in Fig. 10(d) (solid line).

V. DISCUSSION AND CONCLUSIONS

We have reported inelastic neutron-scattering measurements of the powder-averaged spin dynamics in the layered hexagonal antiferromagnet 2H-AgNiO$_2$, which has a collinear alternating stripe-ordered ground state. A broad band of magnetic inelastic scattering is observed above a finite gap indicating strongly dispersive magnetic excitations. The observed modulations in the boundaries of the magnetic scattering could be well explained by a gapped and predominantly two-dimensional dispersion relation, suggesting magnetically weakly coupled triangular layers. For a quantitative analysis we have considered a minimal spin Hamiltonian in Eq. (4) for the localized Ni1 ions ($S=1$) located on an ideal triangular lattice and have neglected the coupling to the itinerant electrons on the surrounding Ni sites. Within this localized model we considered first- and second-neighbor antiferromagnetic couplings J_1 and $J_2=0.15J_1$ in the triangular layers, a strong easy axis anisotropy modeled by a single ion term $\mathcal{D}\simeq 1.3J_1$, and weak interlayer couplings $J_z'=-0.1J_1$ and have found that this minimal model can account quantitatively for all the observed wave-vector dependence of the boundaries of the powder-averaged spectrum.

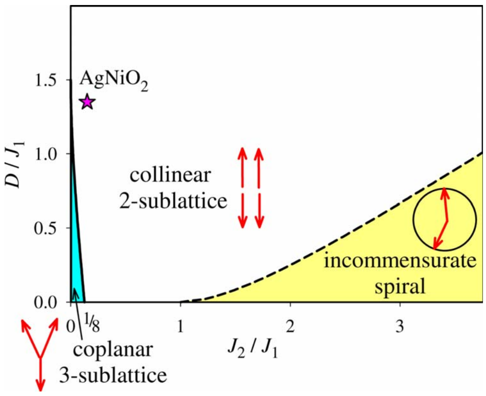

FIG. 14. (Color online) Ground-state phase diagram of the easy-axis Heisenberg model on a triangular lattice as a function of J_2/J_1 and $\mathcal{D}/J_1$, calculated from mean-field theory. The parameters $J_2/J_1 \approx 0.15$, $\mathcal{D}/J_1 \approx 1.3$ deduced from linear spin-wave theory fits to inelastic neutron-scattering data place AgNiO$_2$ within the collinear AF phase, not far from the boundary with a coplanar three-sublattice state.

The deduced values of the magnetic interactions provide a natural explanation for the stability of the observed collinear alternating stripe magnetic order. The large value for the easy-axis anisotropy strongly modifies the physics of an antiferromagnet on a triangular lattice. First, it stabilizes collinear order at the expense of coplanar states like the 120° spiral ground state of a simplest nearest-neighbor Heisenberg model. Second, it opens a gap to spin excitations which strongly suppresses quantum zero-point fluctuations. These are essential for the "order from disorder" selection of collinear order in the *isotropic* J_1-J_2 model considered by Chubukov and Jolicoeur.[3] But in the easy-axis J_1-J_2 model relevant to AgNiO$_2$, fluctuations lead only to small quantitative corrections to the spin-wave dispersion.

We have calculated these corrections explicitly to $\mathcal{O}(1/S)$ and find that, for most purposes, they can safely be neglected as they only lead to a very modest renormalization of the spin-wave dispersion—and the parameters inferred from it—as illustrated in Table I. Competing interactions such as J_2 also play a secondary role, selecting the observed form of collinear order from the vast manifold of Ising ground states on a triangular lattice. The extent of the collinear AF phase as a function of $(J_2/J_1, \mathcal{D}/J_1)$ can easily be estimated within mean-field theory. The results of this analysis are shown in Fig. 14. The parameter set deduced above, with strong anisotropy $\mathcal{D}$ but relatively small second-neighbor interaction J_2, places AgNiO$_2$ within the collinear AF phase—as required—but not far from the boundary with a coplanar three-sublattice state.

At present, the origin of this strong easy-axis anisotropy—which may be of single-ion or exchange character—is unclear. AgNiO$_2$ is a highly anisotropic material, and the crystal fields at the magnetic sites will reflect this. However, relativistic (i.e., spin-orbit coupling) effects in Ni are not usually strong, so the absolute size of anisotropy is surprising. The more massive Ag ions, which have stronger spin-orbit coupling, are nonmagnetic, and thought to play a negligible role in interactions between the Ni^{2+} sites. However, given the partially itinerant nature of Ni electrons, a simple local-moment model such as Eq. (4) is probably unlikely ever to offer a complete description of the magnetism in $AgNiO_2$.

Further band-structure calculations based on the model developed in Ref. 5 could potentially test the proposed minimal Hamiltonian and give further insight into the microscopic origin of the exchange interactions and easy-axis anisotropy. Of particular interest would be the contribution of the itinerant Ni2 and Ni3 sites which surround the strongly magnetic Ni1 sites to magnetic excitations, and their role in mediating interactions between localized Ni1 sites. Even though the dispersions of the boundaries of the powder-averaged data are well explained by Eq. (4), there are discrepancies in the intensity distribution as a function of energy and wave vector [see Fig. 12(E)], and these may contain information about the itinerant electrons. It is also interesting to ask whether the weak but long-range interlayer interaction J_z' could be of RKKY origin. This is a promising avenue for future research, and recent transport experiments on $AgNiO_2$ in high magnetic field reinforce the idea that charge carriers couple strongly to the magnetic order.[16]

Even without these complications, the minimal microscopic model we have proposed has a number of very interesting features. In particular it predicts a spin-wave dispersion with global minima not at magnetic Bragg wave vectors but at symmetry-related soft points. This prediction could be tested by future inelastic neutron-scattering experiments on single crystals or by ESR experiments, which probe the excitations at the Γ point, which by periodicity have the same energy as those at the magnetic Bragg wave vector. We note that the unusual dispersion relation we propose with global minima at multiple soft points may lead to nontrivial magnetically ordered phases in applied magnetic fields that overcome the spin gap and future studies of the phase diagram in high applied magnetic field along the easy axis could show a rich behavior that would be fruitful to explore experimentally[16] and theoretically.[17]

ACKNOWLEDGMENTS

We acknowledge useful discussions with A. V. Chubukov, A. I. Coldea, K. Damle, M. Enderle, L. Seabra, and A. Vishwanath. The research was supported in part by EPSRC-GB U.K. Grants No. GR/R76714/02 (R.C.), No. EP/C51078X/2 (E.W.), and No. EP/C539974/1 (N.S.), a CASE award from the EPSRC-GB and ILL (E.M.W.), and the EU program at the ILL. N.S. and P.A. gratefully acknowledge the support of the guest program of MPI-PKS Dresden, where part of this work was carried out.

APPENDIX A: LINEAR SPIN-WAVE DISPERSIONS FOR COUPLED TRIANGULAR LAYERS

Here we outline the derivation of the linear spin-wave dispersion relations for a model of stacked antiferromagnetic triangular layers with collinear stripe order. The experimentally determined magnetic structure in $2H$-$AgNiO_2$ is shown in Fig. 15. In each triangular Ni layer the ordered spins form alternating ferromagnetic rows described by two magnetic sublattices (up/down), leading to a total of four magnetic sublattices for the two layers in the magnetic unit cell [box in Fig. 15(b)]. After a Holstein-Primakoff transformation from spin to magnon operators and Fourier transformation the spin Hamiltonian in Eq. (4) becomes

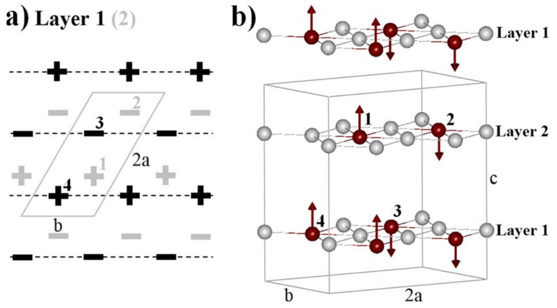

FIG. 15. (Color online) Magnetic structure of $2H$-$AgNiO_2$. (a) In each layer spins form alternating ferromagnetic stripes (dashed lines), ± symbols indicate the projection of the spin moments along the c axis. Stripes are parallel between adjacent layers (thick black symbols for layer 1 and faint gray for layer 2) but have an offset because of the structural arrangement of Ni1 ions. Labels 1–4 refer to the four magnetic sublattices (two for each layer) in the magnetic unit cell (solid contour), which is doubled along a axis compared to the crystallographic unit cell. (b) 3D view of the magnetic structure showing the orientation of the spin moments (thick arrows) of the Ni1 ions (dark brown spheres) in the two layers in the unit cell. Light gray spheres are Ni2 and Ni3 ions, assumed nonmagnetic. The box shows the 3D magnetic unit cell.

$$\mathcal{H} = \sum_{\boldsymbol{q}} \mathbf{X}^{\dagger} H \mathbf{X} + E_0,$$

where E_0 is a constant and terms higher than quadratic are neglected. The sum extends over all wave vectors $\boldsymbol{q}$ in the first magnetic Brillouin zone. The $\boldsymbol{q}$ dependence of the operator matrix $\mathbf{X}$ and of the Hamiltonian matrix H is implicit. The operator matrix $\mathbf{X}^{\dagger}$ is given by

$$\mathbf{X}^{\dagger} = [\alpha_{\boldsymbol{q}}^{\dagger}, \gamma_{\boldsymbol{q}}^{\dagger}, \beta_{-\boldsymbol{q}}, \epsilon_{-\boldsymbol{q}}],$$

where α, β, ϵ, and γ refer to the magnetic sublattices 1, 2, 3, 4 (in this order) and $\alpha_{\boldsymbol{q}}^{\dagger}$ creates a plane-wave magnon mode on sublattice 1, and so on. The Hamiltonian matrix in this operator basis is

$$H = \begin{bmatrix} A & B & C & D^* \\ B^* & A & D & C \\ C & D^* & A & B \\ D & C & B^* & A \end{bmatrix}, \tag{A1}$$

where

$$A = 2S\{J_1 \cos(2\pi k) + J_1 + J_2 \cos[2\pi(2h+k)] + J_2 + J_z' \cos(2\pi l) - J_z' - J_z\} + 2S\mathcal{D}\left(1 - \frac{1}{2S}\right),$$

$$B = 4SJ_z \cos(\pi k)\cos(\pi l)\zeta,$$

$$C = 4SJ_1 \cos(\pi k)\cos[\pi(2h+k)] + 4SJ_2 \cos(3\pi k)\cos[\pi(2h+k)],$$

$$D = 2SJ_z \cos(\pi l)\zeta^2,$$

$$\zeta = e^{-(2h+k)\pi i/3},$$

where (h,k,l) are components of the wave vector $\boldsymbol{q}$ in units of the reciprocal lattice of the hexagonal unit cell shown in Fig. 2(b). Note that the very last term in function A above, $2S\mathcal{D}\times\frac{-1}{2S}$, formally comes in spin-wave theory as a higher order $(1/S)$ correction term, but we have included it here following common convention,[14] since it originates from a quadratic term in boson operators.

Diagonalizing the Hamiltonian in Eq. (A1) using standard methods[15] gives two doubly degenerate modes with dispersions given by

$$(\omega_{\boldsymbol{q}}^{\pm})^2 = A^2 + BB^* - C^2 - DD^* \pm \mathrm{sgn}(B/\zeta)\sqrt{4|AB-CD^*|^2 - |B^*D^* - BD|^2}, \tag{A2}$$

where ± stands for optic and acoustic modes between the two layers and $\mathrm{sgn}(x)$ is the sign function. The above expressions for the dispersion relations also hold by periodicity for a general wave vector $\boldsymbol{Q}=(h,k,l)$ outside the first magnetic Brillouin zone [the two modes are degenerate when $B=0$ and the prefactor $\mathrm{sgn}(B/\zeta)$ in front of the square root is required to ensure continuity of the two distinct modes on both sides of a degenerate point].

For decoupled triangular layers with no anisotropy [$J_z = J_z' = \mathcal{D} = 0$ the dispersion is plotted in Fig. 10(a)] (dashed line) and for the general case is plotted in Fig. 10(c) (dashed and dash-dotted lines). The finite easy-axis anisotropy $\mathcal{D} > 0$ leads to a gap in the spectrum. The gap above the magnetic Bragg peaks increases as a power law with increasing anisotropy $\omega_M^- = 2S\sqrt{\tilde{\mathcal{D}}(4J_1+4J_2+2J_z+\tilde{\mathcal{D}})}$, where $\tilde{\mathcal{D}}=\mathcal{D}(1-\frac{1}{2S})$. However, the gap is near linear in anisotropy at the soft point M', $\omega_{M'}^{\pm} = 2S\sqrt{\tilde{\mathcal{D}}(\tilde{\mathcal{D}}-2J_z)}$, so in the limit of weak couplings between the layers the minimum gap is always at the soft point M' and not at the Bragg wave vector M [see Fig. 10(b)].

The dynamical correlations (per Ni1 spin) are obtained as

$$\begin{aligned} S^{xx}(\boldsymbol{Q},\omega) = {} & \mathcal{C}\frac{S}{8}\left[\frac{|W(-\omega_+)+X(-\omega_+)+Y(-\omega_+)+Z(-\omega_+)|^2}{N(-\omega_+)}\right. \\ & \left. + \frac{|W(\omega_+)+X(\omega_+)+Y(\omega_+)+Z(\omega_+)|^2}{N(\omega_+)}\right]G(\omega-\omega_+) \\ & + \mathcal{C}\frac{S}{8}\left[\frac{|W(-\omega_-)+X(-\omega_-)+Y(-\omega_-)+Z(-\omega_-)|^2}{N(-\omega_-)}\right. \\ & \left. + \frac{|W(\omega_-)+X(\omega_-)+Y(\omega_-)+Z(\omega_-)|^2}{N(\omega_-)}\right]G(\omega-\omega_-) \end{aligned} \tag{A3}$$

where $G(\omega-\omega_\pm)$ is a Gaussian with a finite width to model the instrumental resolution, we use the shorthand notation $\omega_\pm = \omega_{\boldsymbol{Q}}^{\pm}$ and the functions W, X, Y, Z, and N are given by

$$W(\omega) = -(A+\omega)(A^2+BB^*-C^2-DD^*-\omega^2) + 2ABB^* - C(B^*D^*+BD),$$

$$X(\omega) = C(A^2+BB^*-C^2+DD^*-\omega^2) - A(B^*D^*+BD) - \omega(B^*D^*-BD),$$

$$Y(\omega) = B^*[(A+\omega)^2 - BB^* + C^2] - 2C(A+\omega)D + BD^2,$$

$$Z(\omega) = D(A^2+C^2-DD^*-\omega^2) + B^{*2}D^* - 2AB^*C,$$

$$N(\omega) = |-WW^* + XX^* - YY^* + ZZ^*|.$$

The overall intensity prefactor $\mathcal{C}$ in Eq. (A3) is 1 in LSWT and is considered here as a variable parameter in the comparison with the experimental data in order to account (in a first approximation) for a possible overall intensity renormalization compared to LSWT. We note that the above expressions simplify considerably in the absence of the interlayer coupling J_z; in that case the two magnon modes in Eq. (A2) become degenerate with dispersion $\omega_{\boldsymbol{Q}} = \sqrt{A^2-C^2}$ and the dynamical correlations in Eq. (A3) become

$$S^{xx}(\boldsymbol{Q},\omega) = \mathcal{C}\frac{S}{2}\frac{A-C}{\omega}G(\omega-\omega_{\boldsymbol{Q}}). \tag{A4}$$

For completeness we also quote the obtained transformation matrix $\mathcal{S}$ to the normal operator basis $\mathbf{X}' = \mathcal{S}^{-1}\mathbf{X}$ in which the Hamiltonian is diagonal

$$\mathcal{S} = \begin{bmatrix} \bar{W}(\omega_-) & \bar{W}(\omega_+) & \bar{W}(-\omega_-) & \bar{W}(-\omega_+) \\ \bar{Y}(\omega_-) & \bar{Y}(\omega_+) & \bar{Y}(-\omega_-) & \bar{Y}(-\omega_+) \\ \bar{X}(\omega_-) & \bar{X}(\omega_+) & \bar{X}(-\omega_-) & \bar{X}(-\omega_+) \\ \bar{Z}(\omega_-) & \bar{Z}(\omega_+) & \bar{Z}(-\omega_-) & \bar{Z}(-\omega_+) \end{bmatrix},$$

where we use the shorthand notation $\bar{W}(\omega) = W(\omega)/\sqrt{N(\omega)}$ and so on. This matrix satisfies the eigenvalue equation $gH\mathcal{S} = \mathcal{S}gH'$ and the normalization condition $\mathcal{S}g\mathcal{S}^\dagger = g$, where g is the commutator matrix for the operator basis defined by

$$g = \mathbf{X}(\mathbf{X}^*)^T - (\mathbf{X}^*\mathbf{X}^T)^T = \begin{bmatrix} 1 & 0 & 0 & 0 \\ 0 & 1 & 0 & 0 \\ 0 & 0 & -1 & 0 \\ 0 & 0 & 0 & -1 \end{bmatrix}$$

and

$$H' = \begin{bmatrix} \omega_- & 0 & 0 & 0 \\ 0 & \omega_+ & 0 & 0 \\ 0 & 0 & \omega_- & 0 \\ 0 & 0 & 0 & \omega_+ \end{bmatrix}$$

is the Hamiltonian representation in the normal operator basis $\mathbf{X}'$.

The one-magnon neutron-scattering intensity including the polarization factor and the magnetic form factor is

$$S(\boldsymbol{Q},\omega) = (\gamma r_o)^2\left(1+\frac{Q_z^2}{Q^2}\right)\left(\frac{g}{2}f(Q)\right)^2 S^{xx}(\boldsymbol{Q},\omega), \tag{A5}$$

where $(\gamma r_o)^2 = 290.6$ mbarns/sr is a conversion factor to bring the intensity into absolute units of mbarns/meV/sr, $f(Q)$ is the magnetic form factor for Ni^{2+} ions and we take the g factor $g=2$. Q_z is the component of the wave-vector transfer $\boldsymbol{Q}$ along the c axis. A numerical average of Eq. (A5) over a spherical distribution of orientations of the wave-vector transfer $\boldsymbol{Q}$ was performed in order to obtain the orientational-averaged intensity $S(Q,\omega)$ to be compared with the measured powder data.

APPENDIX B: SPIN-WAVE THEORY WITH 1/*S* QUANTUM CORRECTIONS FOR THE EASY-AXIS J_1–J_2 TRIANGULAR ANTIFERROMAGNET

Here we outline calculations of corrections to spin-wave dispersion arising from interactions between magnons at $\mathcal{O}(1/S)$. Calculations to this order have previously been carried out by Chubukov and Jolicoeur[3] for the *isotropic* J_1-J_2 Heisenberg model on a triangular lattice. Here we extend this work to the case of a finite easy-axis anisotropy $\mathcal{D}$. To make contact with this earlier work we use here an orthogonal coordinate system with x along the magnetic stripes and y transverse to stripes in plane as in Fig. 8(b) and label the 2D wave vectors as $(k_x,k_y)=(Q_x a, Q_y a)$, where $Q_{x,y}$ are orthogonal components (in Å^{-1}) and a is the hexagonal lattice parameter.

In the usual linear semiclassical approximation (i.e., neglecting terms which contain more than two Bose operators) we obtain a dispersion

$$\omega_{\boldsymbol{k}} = \sqrt{A_{\boldsymbol{k}}^2 - B_{\boldsymbol{k}}^2},$$

with coefficients

$$A_{\boldsymbol{k}} = 2SJ_1(1+\cos k_x + \alpha + \alpha\cos\sqrt{3}k_y) + 2S\tilde{\mathcal{D}},$$

$$B_{\boldsymbol{k}} = 4SJ_1\cos\frac{\sqrt{3}k_y}{2}\left(\cos\frac{k_x}{2}+\alpha\cos\frac{3k_x}{2}\right), \tag{B1}$$

where $\alpha=J_2/J_1$ and $\tilde{\mathcal{D}}=\mathcal{D}[1-1/(2S)]$. We note that our units differ by an overall factor of two from those in Ref. 3, and that single-ion easy-axis anisotropy contributes terms to the linearized Hamiltonian which are formally of order $\mathcal{O}(1/S)$ relative to usual LSWT.

The leading effect of interactions between spin waves, treated at a one-loop (i.e., Hartree-Fock) level, is to renormalize the coefficients of this dispersion to give

$$\epsilon_{\boldsymbol{k}} = \sqrt{(A_{\boldsymbol{k}}+\delta A_{\boldsymbol{k}})^2 - (B_{\boldsymbol{k}}+\delta B_{\boldsymbol{k}})^2},$$

where

$$\delta A_{\boldsymbol{k}} = \frac{2J_1}{N}\sum_{\boldsymbol{p}}\left[\frac{\bar{A}_{\boldsymbol{p}}-\bar{\omega}_{\boldsymbol{p}}}{2\bar{\omega}_{\boldsymbol{p}}}F(\boldsymbol{k},\boldsymbol{p}) + \frac{\bar{B}_{\boldsymbol{p}}^2}{2\bar{\omega}_{\boldsymbol{p}}}\right],$$

$$\delta B_{\boldsymbol{k}} = -\frac{2J_1}{N}\sum_{\boldsymbol{p}}\left[\frac{\bar{A}_{\boldsymbol{p}}-\bar{\omega}_{\boldsymbol{p}}}{2\bar{\omega}_{\boldsymbol{p}}}\bar{B}_{\boldsymbol{k}} - \frac{\bar{B}_{\boldsymbol{p}}}{2\bar{\omega}_{\boldsymbol{p}}}G(\boldsymbol{k},\boldsymbol{p})\right]. \tag{B2}$$

Here, N is the total number of spins in the triangular plane, and the sum on internal momenta $\boldsymbol{p}$ extends over the entire nuclear Brillouin zone [large thick line hexagon in Fig. 8(a)]. Following Ref. 3, we write $\bar{Z}=Z/(2SJ_1)(Z=A,B,\omega)$ and introduce the functions

$$F(\boldsymbol{k},\boldsymbol{p}) = (1-\cos k_x)(1-\cos p_x) - 2(1+\alpha) + \alpha(1-\cos\sqrt{3}k_y)(1-\cos\sqrt{3}p_y) - \frac{2\mathcal{D}}{J_1},$$

$$\begin{aligned}G(\boldsymbol{k},\boldsymbol{p}) ={}& \cos\frac{\sqrt{3}k_y+k_x}{2}\cos\frac{\sqrt{3}p_y+p_x}{2} + \cos\frac{\sqrt{3}k_y-k_x}{2}\cos\frac{\sqrt{3}p_y-p_x}{2}\\ &+\alpha\left[\cos\frac{\sqrt{3}k_y+3k_x}{2}\cos\frac{\sqrt{3}p_y+3p_x}{2} + \cos\frac{\sqrt{3}k_y-3k_x}{2}\cos\frac{\sqrt{3}p_y-3p_x}{2}\right].\end{aligned} \tag{B3}$$

Anisotropy $\mathcal{D}$ enters $\delta A_{\boldsymbol{k}}$ explicitly through $F(\boldsymbol{k},\boldsymbol{p})$, but its main effect is to introduce a gap into the noninteracting dispersion $\bar{\omega}_{\boldsymbol{k}}$, which acts as an infrared cutoff in *all* denominators. In order not to mix different orders in $1/S$, we set $\tilde{\mathcal{D}}\to\mathcal{D}$ in calculations of $\delta A_{\boldsymbol{k}}$ and $\delta B_{\boldsymbol{k}}$.

To obtain quantitative results for comparison with experiment, the sums in Eq. (B2) were evaluated numerically. The resulting corrections to the linear spin-wave dispersion are illustrated first for the case of no anisotropy in Fig. 10(a) (solid line). In this case we exactly reproduce the results of Ref. 3: LSWT (dashed line) predicts a gapless mode at the soft point M' (as an indirect consequence of the macroscopic classical ground-state degeneracy); however, quantum corrections lift the classical degeneracy by stabilizing the collinear stripe order and generating a spontaneous gap at the soft points while maintaining a gapless Goldstone mode at the magnetic Bragg wave vectors.

In the presence of anisotropy the situation is somewhat different. First the collinear order observed in $\mathrm{AgNiO_2}$ is now stable at a *classical* level for a wide range of $\mathcal{D}$ and J_2 (cf. Fig. 14). And second, *all* spin excitations are now gapped, even in the absence of fluctuation effects [see Fig. 10(b)]. Expanding about collinear order, at a semiclassical level, the gap at the Bragg wave vectors $M=(0,2\pi/\sqrt{3})$ grows as

$$\Delta_M \approx 2S\sqrt{\tilde{\mathcal{D}}(4J_1+4J_2+\tilde{\mathcal{D}})},$$

whereas at the soft points $M'=(\pi,\pi/\sqrt{3})$ it increases only linearly as $2S\tilde{\mathcal{D}}$. As a result, for finite $\mathcal{D}$, the minimum in the spin-wave dispersion occurs on the zone boundary at the soft point M', and *not* at the magnetic ordering vector M. Once $1/S$ corrections are included, a gap is generated dynamically at M' for $\mathcal{D}=0$, and there is a threshold anisotropy value $\mathcal{D}_c$ above which the global minimum gap moves from M to the soft point M'.

For parameters relevant to $2H$-AgNiO$_2$ (see Table I) the gap to spin excitations is large throughout the BZ, with a minimum at M' ($\mathcal{D}_c \approx 0.21$ meV for this parameter set). Quantum fluctuations lead only to small quantitative corrections to the dispersion—compare the dashed to the solid line in Fig. 10(b)—and fits to LSWT are therefore justified *a posteriori*. A further indication that quantum fluctuations are small is the fact that the zero-point reduction in the sublattice magnetization

$$\delta m_{\mathbf{S}} = \frac{2}{N}\sum_{\boldsymbol{p}} \frac{A_{\boldsymbol{p}} - \omega_{\boldsymbol{p}}}{2\omega_{\boldsymbol{p}}} \tag{B4}$$

is calculated to be small: $\delta m_{\mathbf{S}}=0.038$ for the parameters given in Table I.

We note that this is *not* true in the limit of small anisotropy $\mathcal{D}\rightarrow 0$ and small NNN couplings $J_2/J_1 \rightarrow 1/8$, in which case the system is close to a quantum critical point. In this case zero-point fluctuations are very strong and the correction to the sublattice magnetization diverges within LSWT. A consequence of this is that $1/S$ corrections drive the gap

$$\Delta_\Gamma \approx 4\sqrt{(J_1 S + J_2 S)\mathcal{D}[S - 1/2 - \delta m_{\mathbf{S}}]} \tag{B5}$$

at the Γ point $\mathbf{k}=(0,0)$ *imaginary* for a small but finite region of parameters $\mathcal{D}/J_1 \gtrsim 0$, $J_2/J_1 > 1/8$—cf. Fig. 13. Accurate treatment of this small $\mathcal{D}$ regime would require a more sophisticated self-consistent spin-wave theory, which is not warranted for AgNiO$_2$.

For the purposes of comparing the spin-wave calculations at $\mathcal{O}(1/S)$ with the *envelope* of scattering in $(|\boldsymbol{Q}|,\omega)$ it is sufficient to replace $A_{\boldsymbol{k}}$, $B_{\boldsymbol{k}}$, and $\omega_{\boldsymbol{k}}$ by their corrected values in the expression for the scattering intensity

$$S^{xx}(\boldsymbol{Q},\omega) = \mathcal{C}\frac{S}{2}\frac{A_{\boldsymbol{k}} - B_{\boldsymbol{k}}}{\omega_{\boldsymbol{k}}}\delta(\omega - \omega_{\boldsymbol{k}}). \tag{B6}$$

Finally, the interlayer coupling J_z' can easily be included in these calculations by modifying Eq. (B1) as follows:

$$A_{\boldsymbol{k}} \rightarrow A_{\boldsymbol{k}} + 2SJ_z'(\cos k_z - 1).$$

Here $k_z = Q_z c$ where Q_z is the c-axis wave vector component in Å^{-1}. At order $\mathcal{O}(1/S)$ the interlayer couplings modify Eq. (B3) to read

$$F(\boldsymbol{k},\boldsymbol{p}) \rightarrow F(\boldsymbol{k},\boldsymbol{p}) + \frac{J_z'}{J_1}(1 - \cos 2k_z)(1 - \cos 2p_z).$$

However since this change is relatively very small for simplicity we neglect it in the analysis and only consider the explicit effects of J_z' through changes in the dispersion relation at linear order in SWT. The resulting three-dimensional spin-wave dispersion and corrections are shown in Fig. 10(d).

---

*Present address: Helmholtz Centre Berlin for Materials and Energy, Glienicker Str. 100, D-14109 Berlin, Germany.

[1] G. Baskaran, Phys. Rev. Lett. **63**, 2524 (1989).

[2] Th. Jolicoeur, E. Dagotto, E. Gagliano, and S. Bacci, Phys. Rev. B **42**, 4800 (1990).

[3] A. V. Chubukov and Th. Jolicoeur, Phys. Rev. B **46**, 11137 (1992).

[4] P. Lecheminant, B. Bernu, C. Lhuillier, and L. Pierre, Phys. Rev. B **52**, 6647 (1995).

[5] E. Wawrzyńska, R. Coldea, E. M. Wheeler, I. I. Mazin, M. D. Johannes, T. Sörgel, M. Jansen, R. M. Ibberson, and P. G. Radaelli, Phys. Rev. Lett. **99**, 157204 (2007).

[6] J.-H Chung, Th. Proffen, S. Shamoto, A. M. Ghorayeb, L. Croguennec, W. Tian, B. C. Sales, R. Jin, D. Mandrus, and T. Egami, Phys. Rev. B **71**, 064410 (2005).

[7] M. J. Lewis, B. D. Gaulin, L. Filion, C. Kallin, A. J. Berlinsky, H. A. Dabkowska, Y. Qiu, and J. R. D. Copley, Phys. Rev. B **72**, 014408 (2005).

[8] A. Wichainchai, P. Dordor, J. P. Doumerc, E. Marquestaut, M. Pouchard, P. Hagenmuller, and A. Ammar, J. Solid State Chem. **74**, 126 (1988); Y. J. Shin, J. P. Doumerc, P. Dordor, C. Delmas, M. Pouchard, and P. Hagenmuller, *ibid.* **107**, 303 (1993).

[9] T. Sörgel and M. Jansen, Z. Anorg. Allg. Chem. **631**, 2970 (2005).

[10] E. Wawrzyńska, R. Coldea, E. M. Wheeler, T. Sörgel, M. Jansen, R. M. Ibberson, P. G. Radaelli, and M. M. Koza, Phys. Rev. B **77**, 094439 (2008).

[11] P. A. Slotte and P. C. Hemmer, J. Phys. C **17**, 4645 (1984).

[12] F. Ye, J. A. Fernandez-Baca, R. S. Fishman, Y. Ren, H. J. Kang, Y. Qiu, and T. Kimura, Phys. Rev. Lett. **99**, 157201 (2007).

[13] K. Yosida, Prog. Theor. Phys. **6**, 691 (1951).

[14] M. I. Kaganov and A. V. Chubukov, Sov. Phys. Usp. **30**, 1015 (1987).

[15] R. M. White, M. Sparks, and I. Ortenburger, Phys. Rev. **139**, A450 (1965).

[16] A. I. Coldea *et al.* (unpublished).

[17] L. Seabra *et al.* (unpublished).